LETTER

doi:10.1038/nature10505

The crystal structure of an oxygen-tolerant hydrogenase uncovers a novel iron-sulphur centre

Johannes Fritsch[1]*, Patrick Scheerer[2]*, Stefan Frielingsdorf[1], Sebastian Kroschinsky[2], Bärbel Friedrich[1], Oliver Lenz[1] & Christian M. T. Spahn[2,3]

Hydrogenases are abundant enzymes that catalyse the reversible interconversion of H_2 into protons and electrons at high rates[1]. Those hydrogenases maintaining their activity in the presence of O_2 are considered to be central to H_2-based technologies, such as enzymatic fuel cells and for light-driven H_2 production[2]. Despite comprehensive genetic, biochemical, electrochemical and spectroscopic investigations[3–8], the molecular background allowing a structural interpretation of how the catalytic centre is protected from irreversible inactivation by O_2 has remained unclear. Here we present the crystal structure of an O_2-tolerant [NiFe]-hydrogenase from the aerobic H_2 oxidizer *Ralstonia eutropha* H16 at 1.5 Å resolution. The heterodimeric enzyme consists of a large subunit harbouring the catalytic centre in the H_2-reduced state and a small subunit containing an electron relay consisting of three different iron-sulphur clusters. The cluster proximal to the active site displays an unprecedented [4Fe-3S] structure and is coordinated by six cysteines. According to the current model, this cofactor operates as an electronic switch depending on the nature of the gas molecule approaching the active site. It serves as an electron acceptor in the course of H_2 oxidation and as an electron-delivering device upon O_2 attack at the active site. This dual function is supported by the capability of the novel iron-sulphur cluster to adopt three redox states at physiological redox potentials[7–9]. The second structural feature is a network of extended water cavities that may act as a channel facilitating the removal of water produced at the [NiFe] active site. These discoveries will have an impact on the design of biological and chemical H_2-converting catalysts that are capable of cycling H_2 in air.

More than two billion years ago, ancient microbes exploited the reducing power of H_2 for their metabolism; until today H_2 provides a valuable energy source which is used by H_2-oxidizing uptake hydrogenases. The reverse process, that is, the liberation of H_2, serves as safety valve to eliminate excessive reducing power under anaerobic conditions. This proton reduction reaction is catalysed by the group of H_2-evolving hydrogenases. All hydrogenases use abundant transition metals such as nickel and iron for catalysis, contrary to man-made H_2-converting catalysts that predominantly rely on rare precious metals.

Among three phylogenetically distinct types of hydrogenases, two enzyme classes prevail in nature. According to the metal content of their active sites they are classified as nickel-iron ([NiFe]) and di-iron ([FeFe]) hydrogenases[10]. [FeFe]-hydrogenases are highly productive in H_2 evolution, but are irreversibly inactivated during catalysis by even trace amounts of O_2 (ref. 11). [NiFe]-hydrogenases, however, function usually in the direction of H_2 oxidation and are less sensitive to O_2. In most cases, O_2 reacts with the active site giving rise to a mixture of inactive states, denoted as Ni-A and Ni-B, depending on the nature of the oxygen ligand bridging the Ni and Fe atoms in the active site[12]. Both inactive forms, however, can be reactivated under reducing conditions. Enzymes in the Ni-B state reactivate rapidly, whereas the recalcitrant Ni-A state requires long-term reactivation that may occur exclusively *in vitro*[13,14]. Consequently, a prerequisite for a hydrogenase to function *in vivo* in the presence of O_2 is the strict avoidance of the Ni-A form and a continuous removal of the oxygen species related to the Ni-B state. These features are present in a small group of [NiFe]-hydrogenases that are designed to operate in mixtures of H_2 and O_2 (ref. 15). Knallgas bacterium *Ralstonia eutropha* H16 harbours at least three [NiFe]-hydrogenases capable of oxidizing H_2 at atmospheric p_{O_2}. The best-characterized enzyme is the heterodimeric membrane-bound [NiFe]-hydrogenase (MBH), which is attached to the periplasmic side of the cytoplasmic membrane and feeds the electrons derived from H_2 oxidation via a membrane-integral *b*-type cytochrome directly into the respiratory chain (Fig. 1)[16]. Recent studies suggested that the iron-sulphur (Fe-S) cluster in the proximal position to the [NiFe] active site of MBH significantly differs in its electronic structure and function from conventional [4Fe-4S] cubanes, which are usually located at the corresponding position of O_2-sensitive [NiFe]-hydrogenases[4,7]. Moreover, experimental evidence revealed that this particular cluster

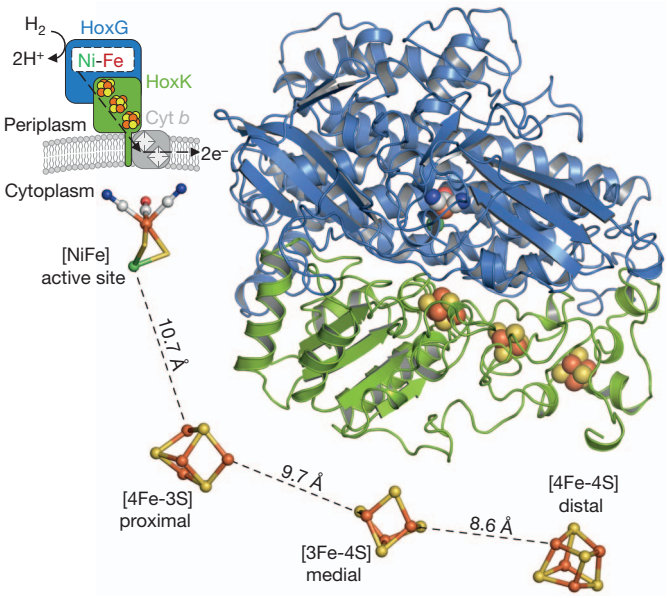

Figure 1 | Overall structure of the membrane-bound hydrogenase from *R. eutropha*. The upper-left inset is a cartoon depiction of the cellular localization of MBH. Electrons from H_2 oxidation are transferred through a relay of Fe-S clusters via a *b*-type cytochrome (Cyt *b*) to the respiratory chain. The ribbon representation shows the large (blue) and small (green) subunits of MBH. The catalytic centre and the three Fe-S clusters are symbolized as spheres. The spatial arrangement of MBH cofactors is illustrated in ball-and-stick representation in the lower part of the figure.

[1]Mikrobiologie, Institut für Biologie, Humboldt-Universität zu Berlin, Chausseestraße 117, 10115 Berlin, Germany. [2]Institut für Medizinische Physik und Biophysik (CC2), Charité–Universitätsmedizin Berlin, Charitéplatz 1, 10117 Berlin, Germany. [3]Zentrum für Biophysik und Bioinformatik, Humboldt-Universität zu Berlin, Invalidenstraße 42, 10115 Berlin, Germany.
*These authors contributed equally to this work.

has a crucial role in the O_2 tolerance of MBH[7]. However, all structural interpretations of O_2 tolerance have been made on the basis of crystal structures from O_2-sensitive [NiFe]-hydrogenases[12,17–20].

To solve the crystal structure of MBH, the heterodimeric enzyme was purified from the solubilized membrane fraction of *R. eutropha* cells according to an optimized cultivation and purification protocol resulting in highly active and homogeneous protein preparations[7]. Dark-brown MBH crystals were harvested under a reducing atmosphere containing 5% H_2 and 95% N_2. The structure was solved by molecular replacement using the structure of the reduced hydrogenase of *Desulfovibrio vulgaris* Miyazaki F (Protein Data Bank accession 1WUL) as the search template, and the model was refined to a resolution of 1.5 Å.

The two MBH subunits show the typical overall topology of crystallized O_2-sensitive [NiFe]-hydrogenases (Fig. 1 and Supplementary Figs 1 and 2)[12,17–20]. An initial omit electron density map readily uncovered the catalytic centre in the large subunit and the three Fe-S clusters in the small subunit (Supplementary Fig. 3). All four cofactors are spaced in distances of approximately 10 Å that allow electron transfer at physiologically relevant rates (Fig. 1). The bimetallic active site of MBH consists of a nickel atom coordinated by four cysteines, two of which are bridging ligands to the iron atom (Fig. 2a). Furthermore, the iron carries three diatomic ligands, one carbonyl (CO) and two cyanide (CN^-) groups. The distance of 2.6 Å between the two metal atoms agrees with the reduced conformation of the active site[12]. Consistent with previous spectroscopic observations[4,7], the first coordination sphere of the MBH catalytic centre is very similar to that of O_2-sensitive [NiFe]-hydrogenases (Supplementary Fig. 4). This indicates that the O_2 tolerance of MBH does not rely on a significant modification of the catalytic centre[7].

Three Fe-S clusters in the MBH small subunit conduct the electron flow between the [NiFe]-active site and the cytochrome *b* (Fig. 1). The distal cluster relative to the active site is a cuboidal [4Fe-4S] centre coordinated by three cysteines and one histidine (Fig. 2d). It is shielded from the solvent by a 3_{10}-helix representing the first part of the carboxy-terminal α-helical extension of HoxK (Fig. 1 and Supplementary Fig. 1), which is essential for both anchoring the hydrogenase to the membrane and a tight connection to cytochrome *b*[16]. Three cysteine residues are involved in coordination of a [3Fe-4S] cluster which occupies the medial position, as observed in other [NiFe]-hydrogenases[17,18,20] (Fig. 2c). The most surprising feature of MBH was observed at the position proximal to the active site. Instead of a common [4Fe-4S] cluster, a novel type of Fe-S cluster was found comprising four iron atoms but only three sulphides (Fig. 2b and Supplementary Fig. 3c). The conformation of this unprecedented [4Fe-3S] cluster is maintained by four cysteines (Cys 17^S, Cys 20^S, Cys 115^S, Cys 149^S, where S indicates the small subunit), which are conserved in all [NiFe]-hydrogenases, and two additional cysteines (Cys 19^S, Cys 120^S) exclusively found in O_2-tolerant enzymes (Supplementary Fig. 5)[6–8]. In fact, Cys 19^S and Cys 120^S ligate three of the four iron atoms resulting in an open distorted conformation of the cluster (Fig. 3). In a concerted manner, Cys 120^S and Cys 149^S withdraw Fe3 from the cuboidal structure resulting in enlarged Fe–Fe distances of 3.5 and 4.0 Å to Fe1 and Fe4, respectively (Fig. 3). Notably, the typical Fe–Fe distance in [4Fe-4S] and [3Fe-4S] clusters is 2.7 Å (refs 17, 18, 20). The position of the missing sulphide in the [4Fe-3S] cluster, compared to a [4Fe-4S] centre, is occupied by the thiolate sulphur of Cys 19^S (Fig. 3).

The [4Fe-3S] cluster is clearly distinct from distorted, partially damaged clusters found in crystal structures of some standard hydrogenases[19,20]. Moreover, it is unique among Fe-S centres with unusual structures (Supplementary Fig. 6). Surprisingly, the MBH proximal cluster shares similarity with one half of the reduced P-cluster of nitrogenase[21]. The P-cluster resembles a tandem of two cuboidal 4Fe-3S modules bridged by a single sulphide[22]. The resulting [8Fe-7S] centre is coordinated by six cysteine residues, two of which serve as bridging ligands. Interestingly, one of the two 4Fe-3S modules was found in a highly distorted conformation, which is analogous to the structure of the [4Fe-3S] cluster in MBH (Fig. 3 and Supplementary Fig. 6).

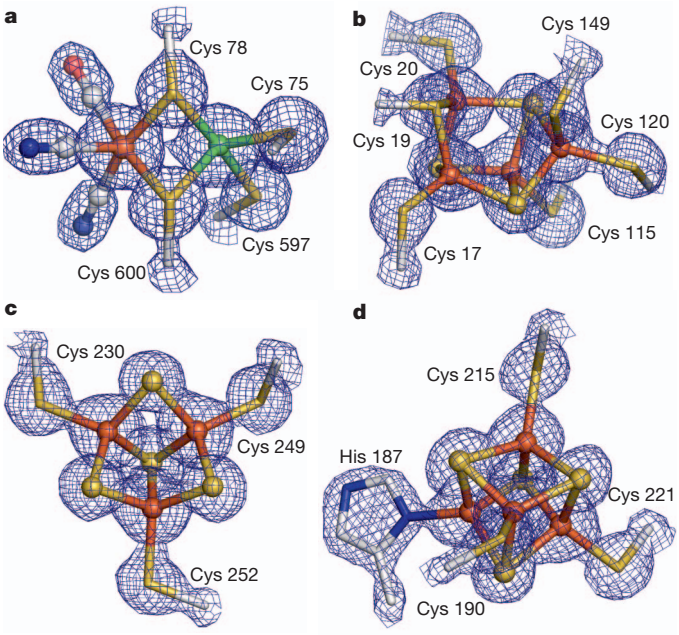

Figure 2 | Metal cofactors of the MBH. The blue meshes represent $2F_o - F_c$ electron densities contoured at 2.0σ. **a**–**d**, The $2F_o - F_c$ electron densities perfectly fit with the $[(CysS)_2Ni(\mu\text{-}CysS)_2Fe(CN)_2(CO)]$ centre (**a**), a proximal [4Fe-3S] cluster coordinated by six cysteine-derived sulphurs (**b**), a medial [3Fe-4S] cluster coordinated by three cysteine residues (**c**), and a distal [4Fe-4S] cluster coordinated by three cysteine residues and one histidine (**d**). All cofactors are shown in ball-and-stick representation; the coordinating amino acid side chains are depicted as stick models.

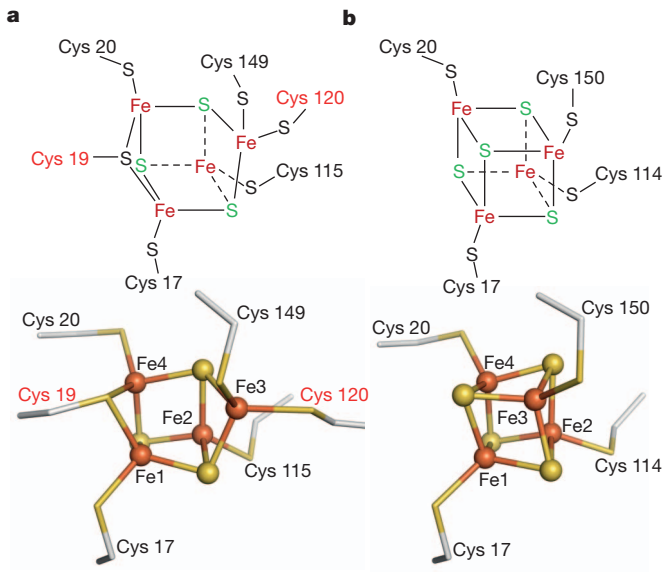

Figure 3 | Architecture of the proximal [4Fe-3S] cluster. **a**, Schematic model and structure of the [4Fe-3S] cluster and the corresponding coordinating cysteine ligands in the MBH small subunit. **b**, The proximal [4Fe-4S] cluster of the O_2-sensitive standard [NiFe]-hydrogenase from *D. vulgaris* Miyazaki F (Protein Data Bank accession 1WUL). In the upper schemes, the sulphides and cysteine-derived sulphur atoms are labelled in green and black, respectively. The cluster structures are shown in ball-and-stick representation; the coordinating amino acid side chains are depicted as stick models.

Oxygen tolerance implies that, upon approaching the catalytic centre, O_2 has to be removed reductively through an immediate delivery of four electrons and protons for the complete reduction of O_2 to water[5,7]. Because the oxidized active site is blocked and cannot bind H_2, electrons must be delivered by reverse electron flow[3,5,7,16]. This feature seems to be linked to the previously determined, comparatively high redox potentials of the Fe-S clusters in MBH, which range from −180 mV to +160 mV. Moreover, the proximal cluster alone appears to undergo two redox transitions within an extraordinary narrow potential window from −60 mV to +160 mV (refs 4, 7, 9, 16, 23). The unique capability to carry two electrons at the same time at physiologically relevant potentials is in perfect agreement with the precisely assigned redox transitions mediated by the Fe-S clusters of the O_2-tolerant, MBH-related hydrogenase I from *Aquifex aeolicus*[8]. Generally, the potential range between the 3+/2+ and 2+/1+ transitions of high-potential as well as ferredoxin-type [4Fe-4S] clusters is approximately 1,000 mV, placing either of the transitions beyond physiological relevance[24,25]. However, the corresponding potential window of the two redox transitions mediated by the [4Fe-3S] cluster is only 220 mV (refs 8, 9, 23).

Compared to the rather symmetric [4Fe-4S] clusters, the four iron atoms of the [4Fe-3S] cluster are coordinated by a higher number of cysteine-derived thiolates and a lower number of sulphides (Fig. 3). This structural information in combination with the interpretation of data from interdisciplinary studies[3–5,7] suggest that three out of four iron atoms reside formally in the 3+ state in the most oxidized form of the [4Fe-3S] cluster, which has been substantiated by Mössbauer experiments performed on hydrogenase I from *A. aeolicus*[8]. According to the current understanding[26,27], the increased thiolate:sulphide ratio elevates the redox potentials of all redox transitions mediated by an Fe-S cluster. In the case of the [4Fe-3S] cluster, this would explain the high value of −60 mV of the low-potential redox transition, but certainly not the relatively low value of the high-potential redox transition (E_M = +160 mV). Conventional high-potential [4Fe-4S] clusters are embedded in a hydrophobic pocket. Consequently, the number of hydrogen bonds (particularly those from water molecules) to sulphur ligands is low, which in turn leads to a high covalency of the Fe-S bonds and poises the 3+/2+ transition to a physiological potential range[26–29]. A conserved water molecule in O_2-sensitive hydrogenases is replaced by the Cys 120^S thiolate sulphur. However, two well-defined water molecules (Wat366, Wat447, Supplementary Fig. 3b) were found within hydrogen-bonding distance to the [4Fe-3S] cluster. This leaves the question open as to how the protein environment tunes the high-potential transition of the proximal [4Fe-3S] cluster. Notably, the open conformation of the [4Fe-3S] cluster provides enhanced structural flexibility permitting redox-dependent rearrangements which have been observed, for example, for the P-cluster of nitrogenase[22]

As discussed above, H_2 conversion in the presence of O_2 implies continuous production of H_2O at the active site[5,7,16]. Thus, H_2O needs to be continuously removed from the protein core to the surface. It is rather unlikely that H_2O molecules escape through the proposed hydrophobic gas channels[30], which are also observed in MBH (Supplementary Fig. 7). The structure of MBH uncovered water-filled cavities that connect the active site with the solvent (Fig. 4) and are absent in the crystal structures of O_2-sensitive [NiFe]-hydrogenases (Supplementary Fig. 8). The additional cavity close to Cys 81^L (where L indicates the large subunit) in MBH originates from the replacement of a bulky tyrosine, present in most O_2-sensitve hydrogenases (Supplementary Fig. 5), by the small Gly 80^L residue. Two gates on opposite sides of this water pocket seem to prevent unrestricted water/proton flow between the active site and the protein surface. The imidazol group of His 220^L, which is conserved in O_2-tolerant hydrogenases and the presence of which strictly correlates with the occurrence of Gly 80^L, disrupts the direct connection to a water-filled extension of the gas channel that reaches the [NiFe] centre (Fig. 4). The proposed water transfer to the surface is gated by salt bridges formed between

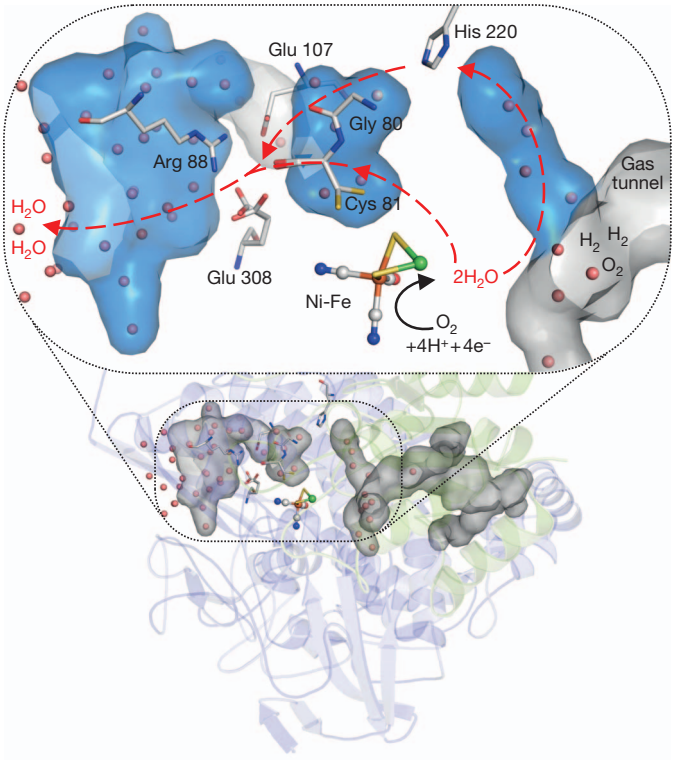

Figure 4 | Proposed water/proton transfer pathway from the MBH active site to the protein surface. Relevant water-filled cavities are coloured in blue; the water molecules are represented as red spheres. Other cavities including the mostly hydrophobic gas channel[30] are shown in grey. Amino acids in the large subunit involved in the proposed water/proton transfer (red arrows) are depicted as sticks. Cys 81^L and Glu 308^L are shown in both side-chain conformations (see also Supplementary Fig. 9). For the complete reduction of O_2 to two H_2O molecules, four electrons must be delivered rapidly by the electron relay of the small subunit (Supplementary Fig. 7).

Arg 88^L and the glutamate residues, Glu 107^L and Glu 308^L (Fig. 4). Remarkably, we identified two rotamers of Glu 308^L, indicating a transient opening of the gate (Supplementary Fig. 9). Thus, the structural data are compatible with a controlled translocation of water molecules, probably with accompanied proton transfer, supporting the model that O_2-tolerant hydrogenases form water as a catalytic by-product during H_2 conversion in the presence of O_2.

METHODS SUMMARY

Crystallization and structure determination of MBH. The membrane fraction containing *Strep*-tagged MBH was prepared from *R. eutropha* cells grown heterotrophically under microaerobic, hydrogenase-derepressing conditions[7]. After treatment with $K_3[Fe(CN)_6]$, membrane proteins were solubilized with Triton X-114, and MBH was purified via *Strep*-Tactin affinity chromatography. MBH crystals were obtained using sitting-drop vapour diffusion. On a microbridge, 8 µl protein solution containing 0.1 mM MBH were mixed with 8 µl of reservoir solution containing 20–30% PEG3350, and 0.1 M Bis-(2-hydroxy-ethyl)-amino-tris(hydroxymethyl)-methane, pH 5.5–6.5. Crystals of MBH grew to full size in the drops within 5 days. The crystals were directly frozen in liquid nitrogen for screening and X-ray analysis at the synchrotron ESRF, Grenoble (France).

Full Methods and any associated references are available in the online version of the paper at www.nature.com/nature.

Received 11 April; accepted 23 August 2011.
Published online 16 October 2011.

1. Cammack, R., Frey, M. & Robson, R. *Hydrogen as a Fuel, Learning from Nature* (Taylor & Francis, 2001).
2. Friedrich, B., Fritsch, J. & Lenz, O. Oxygen-tolerant hydrogenases in hydrogen-based technologies. *Curr. Opin. Biotechnol.* **22,** 358–364 (2011).

3. Ludwig, M., Cracknell, J. A., Vincent, K. A., Armstrong, F. A. & Lenz, O. Oxygen-tolerant H_2 oxidation by membrane-bound [NiFe] hydrogenases of *Ralstonia* species. Coping with low level H_2 in air. *J. Biol. Chem.* **284,** 465–477 (2009).
4. Saggu, M. *et al.* Spectroscopic insights into the oxygen-tolerant membrane-associated [NiFe] hydrogenase of *Ralstonia eutropha* H16. *J. Biol. Chem.* **284,** 16264–16276 (2009).
5. Cracknell, J. A., Wait, A. F., Lenz, O., Friedrich, B. & Armstrong, F. A. A kinetic and thermodynamic understanding of O_2 tolerance in [NiFe]-hydrogenases. *Proc. Natl Acad. Sci. USA* **106,** 20681–20686 (2009).
6. Lukey, M. J. *et al.* How *Escherichia coli* is equipped to oxidize hydrogen under different redox conditions. *J. Biol. Chem.* **285,** 3928–3938 (2010).
7. Goris, T. *et al.* A unique iron-sulfur cluster is crucial for oxygen tolerance of a [NiFe]-hydrogenase. *Nature Chem. Biol.* **7,** 310–318 (2011).
8. Pandelia, M. E. *et al.* Characterization of a unique [FeS] cluster in the electron transfer chain of the oxygen tolerant [NiFe] hydrogenase from *Aquifex aeolicus*. *Proc. Natl Acad. Sci. USA* **108,** 6097–6102 (2011).
9. Schneider, K., Patil, D. S. & Cammack, R. Electron-spin-resonance properties of membrane-bound hydrogenases from aerobic hydrogen bacteria. *Biochim. Biophys. Acta* **748,** 353–361 (1983).
10. Vignais, P. M. & Billoud, B. Occurrence, classification, and biological function of hydrogenases: an overview. *Chem. Rev.* **107,** 4206–4272 (2007).
11. Stripp, S. T. *et al.* How oxygen attacks [FeFe] hydrogenases from photosynthetic organisms. *Proc. Natl Acad. Sci. USA* **106,** 17331–17336 (2009).
12. Ogata, H., Lubitz, W. & Higuchi, Y. [NiFe] hydrogenases: structural and spectroscopic studies of the reaction mechanism. *Dalton Trans.* 7577–7587 (2009).
13. Vincent, K. A., Parkin, A. & Armstrong, F. A. Investigating and exploiting the electrocatalytic properties of hydrogenases. *Chem. Rev.* **107,** 4366–4413 (2007).
14. De Lacey, A. L., Fernandez, V. M., Rousset, M. & Cammack, R. Activation and inactivation of hydrogenase function and the catalytic cycle: spectroelectrochemical studies. *Chem. Rev.* **107,** 4304–4330 (2007).
15. Schwartz, E. & Friedrich, B. in *The Prokaryotes* (eds Dworkin, M. *et al.*) 496–563 (Springer, 2006).
16. Lenz, O. *et al.* H_2 conversion in the presence of O_2 as performed by the membrane-bound [NiFe]-hydrogenase of *Ralstonia eutropha*. *ChemPhysChem* **11,** 1107–1119 (2010).
17. Volbeda, A. *et al.* Crystal structure of the nickel-iron hydrogenase from *Desulfovibrio gigas*. *Nature* **373,** 580–587 (1995).
18. Volbeda, A. *et al.* Structural differences between the ready and unready oxidized states of [NiFe] hydrogenases. *J. Biol. Inorg. Chem.* **10,** 239–249 (2005).
19. Matias, P. M. *et al.* [NiFe] hydrogenase from *Desulfovibrio desulfuricans* ATCC 27774: gene sequencing, three-dimensional structure determination and refinement at 1.8 Å and modelling studies of its interaction with the tetrahaem cytochrome c_3. *J. Biol. Inorg. Chem.* **6,** 63–81 (2001).
20. Ogata, H., Kellers, P. & Lubitz, W. The crystal structure of the [NiFe] hydrogenase from the photosynthetic bacterium *Allochromatium vinosum*: characterization of the oxidized enzyme (Ni-A state). *J. Mol. Biol.* **402,** 428–444 (2010).
21. Seefeldt, L. C., Hoffman, B. M. & Dean, D. R. Mechanism of Mo-dependent nitrogenase. *Annu. Rev. Biochem.* **78,** 701–722 (2009).
22. Peters, J. W. *et al.* Redox-dependent structural changes in the nitrogenase P-cluster. *Biochemistry* **36,** 1181–1187 (1997).
23. Knüttel, K. *et al.* Redox properties of the metal centers in the membrane-bound hydrogenase from *Alcaligens eurtophus* CH34. *Bull. Polish Acad. Sci.* **42,** 495–511 (1994).
24. Cammack, R. ''Super-reduction'' of chromatium high-potential iron-sulphur protein in the presence of dimethyl sulphoxide. *Biochem. Biophys. Res. Commun.* **54,** 548–554 (1973).
25. Thomson, A. J. *et al.* Low-temperature magnetic circular-dichroism evidence for the conversion of 4-iron-sulfur clusters in a ferredoxin from *Clostridium pasteurianum* into 3-iron-sulfur clusters. *Biochim. Biophys. Acta* **637,** 423–432 (1981).
26. Capozzi, F., Ciurli, S. & Luchinat, C. Coordination sphere versus protein environment as determinants of electronic and functional properties of iron-sulfur proteins. *Metal Sites Proteins Models* **90,** 127–160 (1998).
27. Carter, C. W. Jr. New stereochemical analogies between iron-sulfur electron transport proteins. *J. Biol. Chem.* **252,** 7802–7811 (1977).
28. Dey, A. *et al.* Solvent tuning of electrochemical potentials in the active sites of HiPIP versus ferredoxin. *Science* **318,** 1464–1468 (2007).
29. Heering, H. A., Bulsink, B. M., Hagen, W. R. & Meyer, T. E. Influence of charge and polarity on the redox potentials of high-potential iron-sulfur proteins: evidence for the existence of two groups. *Biochemistry* **34,** 14675–14686 (1995).
30. Montet, Y. *et al.* Gas access to the active site of Ni-Fe hydrogenases probed by X-ray crystallography and molecular dynamics. *Nature Struct. Biol.* **4,** 523–526 (1997).

Supplementary Information is linked to the online version of the paper at www.nature.com/nature.

Acknowledgements We are grateful to U. Müller, M. Weiss and the scientific staff of the BESSY-MX/Helmholtz Zentrum Berlin für Materialien und Energie at beamlines BL 14.1 and BL 14.2, D. von Stetten and A. Royant of the ID29S-Cryobench (ESRF, Grenoble) and the European Synchrotron Radiation Facility (ESRF, Grenoble) at beamlines ID23-1, ID23-2, ID14-1 and ID 14-4, where the data were collected, for support. This work was supported by the EU/FP7 programme Solar-H2 (to J.F.), the DFG Cluster of Excellence 'Unifying Concepts in Catalysis' (to S.F., B.F., O.L.), and the Sfb740 (to C.M.T.S.). P.S. acknowledges K. P. Hofmann and his advanced investigator ERC grant (ERC-2009/249910—TUDOR) for support.

Author Contributions J.F. and P.S. are joint first authors. J.F. optimized cell growth conditions as well as the MBH purification procedure. P.S. conducted the crystallization screening; P.S., J.F. and S.F. optimized MBH crystallization conditions. P.S. and S.K. collected the X-ray diffraction data. P.S. performed data processing, solved and refined the MBH structure. B.F., O.L. and P.S. coordinated the project. J.F., P.S., S.F. and O.L. analysed data. J.F., P.S., S.F., B.F., O.L. and C.M.T.S. wrote the manuscript.

Author Information Atomic coordinates and structure factors for the reported structure have been deposited in the Protein Data Bank with the accession code 3RGW. Reprints and permissions information is available at www.nature.com/reprints. The authors declare no competing financial interests. Readers are welcome to comment on the online version of this article at www.nature.com/nature. Correspondence and requests for materials should be addressed to P.S. (patrick.scheerer@charite.de), O.L. (oliver.lenz@cms.hu-berlin.de) or C.M.T.S. (christian.spahn@charite.de).

METHODS

Media and cell growth conditions. Basic media and growth conditions for *R. eutropha* have been described previously[7,31]. *Ralstonia eutropha* HF649 was cultivated heterotrophically at 30 °C in a modified FGN mineral medium containing 0.04% wt/vol fructose, 0.4% wt/vol glycerol and 40 μM $FeCl_3$. 4,000 ml cultures were shaken in baffled 5,000 ml Erlenmeyer flasks at 120 r.p.m. under air until they reached an optical density at 436 nm of 12 ± 1. Cells were harvested by centrifugation at 6,000*g* for 15 min at 4 °C.

Isolation of membranes and *Strep*-Tactin affinity chromatography. Fractionation and purification steps were performed at 4 °C. Cells were re-suspended in buffer (3 ml 65 mM potassium phosphate [K-PO_4], 300 mM NaCl, pH 7.0, per 1 g wet weight) containing Complete EDTA-free protease inhibitor cocktail (Roche Applied Science) and DNase I. The cell suspension was subsequently disrupted in a French pressure cell (SLM Aminco) via two passages at 1,241 bar. The resulting crude extract was treated by sonication (Branson Sonifier) and the cell debris was removed by low-speed centrifugation (4,000*g*, 30 min). $K_3[Fe(CN)_6]$ was added to the crude extract at a final concentration of 50 mM. Membrane and soluble fractions were separated by ultracentrifugation (100,000*g* for 60 min). The membrane pellet was washed with re-suspension buffer containing Complete protease inhibitor cocktail (Roche Applied Science), followed by ultracentrifugation (100,000*g* for 50 min). Membrane proteins were solubilized in 10 ml buffer (65 mM K-PO_4, 300 mM NaCl, 2% wt/vol Triton X-114, Complete protease inhibitor cocktail, pH 7.02) per 1 g of membrane pellet by stirring on ice for 2 h. After ultracentrifugation (100,000*g*, 45 min), the supernatant containing the solubilized membrane extract was loaded onto *Strep*-Tactin Superflow columns (IBA) which were run by gravity flow. To remove unbound proteins, the columns were washed with 12 bed volumes of re-suspension buffer and proteins were eluted with buffer containing 50 mM K-PO_4, 150 mM NaCl, 5 mM desthiobiotin and 10% wt/vol glycerol at pH 7. MBH-containing fractions were pooled, concentrated and the buffer was exchanged to 40 mM K-PO_4, 150 mM NaCl, 10% wt/vol glycerol, pH 5.5, with a centrifugal filter device (Amicon Ultra-15 PL-30, Millipore). Protein concentrations were determined with the BCA-kit (Pierce) with bovine serum albumin as standard.

Hydrogenase activity assay. Spectrophotometric activity measurements of purified MBH were conducted at 30 °C in a rubber-stoppered cuvette containing H_2-saturated K-PO_4 buffer (50 mM, pH 5.5) and methylene blue as the electron acceptor[32].

Crystallization. MBH was used for crystallization at concentrations up to 14 mg ml^{-1} (7–14 mg ml^{-1}). Crystallization screens by the sparse matrix method[33] were carried out by the sitting-drop vapour diffusion method testing more than 1,000 crystallization conditions at 277 K and 291 K using 96-well MRC plates. Promising conditions were systematically screened further by changing protein concentration, pH and the concentration of precipitation agents. Optimized MBH crystals could be grown by sitting-drop vapour diffusion method at 282 K using 24-well Linbro plates. Each sitting drop was prepared on a microbridge by mixing equal volumes (8 μl each) of MBH and reservoir solution. The reservoir solution contained 20–30% polyethylene glycol 3350, 100 mM Bis-(2-hydroxy-ethyl)-amino-tris(hydroxymethyl)-methane buffer, pH 5.5–6.5. Dark-brown MBH crystals appeared within 1–2 days and grew further for 4–5 days and were harvested under an atmosphere composed of 5% H_2 and 95% N_2. MBH crystals were flash frozen in liquid nitrogen with (90% (v/v) reservoir solution and 10% (w/v) polyethylene glycol 400) and without further cryoprotection. Fully grown crystals had dimensions of approximately $1.4 \times 0.3 \times 0.3\ mm^3$. Dissolved MBH crystals exhibited the same H_2 oxidation activity of 130 μmol H_2 per min per mg of protein as the protein before crystallization, demonstrating that the crystallization process preserved the catalytic activity of the enzyme.

Structure analysis. Diffraction data collection was performed at 100 K using synchrotron X-ray sources at ESRF, Grenoble, France, and BESSY II, Berlin, Germany. Best diffraction data were collected at beamline ID14-4 at ESRF, at λ = 0.9395 Å. The crystal to ADSC Q315r detector distance was fixed at 127.8 mm for MBH. The rotation increment for each frame was 0.5° with an exposure time of 1 s. To reduce significantly the radiation damage on the crystal we used the helical data collection protocol at beamline ID14-4[34]. All images were indexed, integrated and scaled using the XDS program package[35] and CCP4 program SCALA[36,37]. Crystals belong to orthorhombic space group $P2_12_12_1$ ($a = 73.09$ Å, $b = 95.65$ Å, $c = 119.15$ Å, $\alpha = \beta = \gamma = 90°$). Supplementary Table 1 summarizes the statistics for crystallographic data collection and structural refinement.

Initial phases for MBH in the H_2-reduced state were obtained by conventional molecular replacement protocol (rotation, translation, rigid body fitting) using the [NiFe]-hydrogenase structure of *Desulfovibrio vulgaris* (Protein Data Bank accession 1WUL) as the initial search model. Molecular replacement was achieved using the CCP4 program PHASER[37,38] by first placing the MBH heterodimer (rotation function [RFZ]: $Z = 21.7$; translation function [TFZ]: $Z = 36.2$ for MBH; RFZ and TFZ as defined by PHASER). In subsequent steps, torsion angle molecular dynamics, simulated annealing using a slow-cooling protocol and a maximum likelihood target function, energy minimization, and B-factor refinement by the program CNS[39] were carried out in the resolution range 74.6–1.5 Å. After the first round of refinement, all [Fe_n-S_n] clusters and [NiFe]-active site were clearly visible in the electron density of both σA-weighted $2F_o - F_c$ maps, as well as in the σA-weighted simulated annealing omitted density maps (Supplementary Fig. 3). Restrained, individual B-factors were refined and the crystal structure was finalized by the CCP4 program REFMAC5 and CCP4[37,40] and PHENIX[41]. The final model has agreement factors R_{free} and R_{cryst} of 15.2% and 13.9%. Manual rebuilding of the MBH model and electron density interpretation was performed after each refinement cycle using the program COOT[42]. Structure validation was performed with the programs PROCHECK[43] and WHAT_CHECK[44]. Potential hydrogen bonds and van der Waals contacts were analysed using the programs HBPLUS[45] and LIGPLOT[46]. All crystal structure superpositions of backbone α carbon traces were performed using the CCP4 program LSQKAB[37]. The solvent-accessible area was calculated using the PISA Server[47]. All molecular graphics representations were created using PyMol[48].

31. Schubert, T., Lenz, O., Krause, E., Volkmer, R. & Friedrich, B. Chaperones specific for the membrane-bound [NiFe]-hydrogenase interact with the Tat signal peptide of the small subunit precursor in *Ralstonia eutropha* H16. *Mol. Microbiol.* **66,** 453–467 (2007).
32. Schink, B. & Schlegel, H. G. The membrane-bound hydrogenase of *Alcaligenes eutrophus*. I. Solubilization, purification, and biochemical properties. *Biochim. Biophys. Acta* **567,** 315–324 (1979).
33. Jancarik, J. & Kim, S.-H. Sparse matrix sampling: a screening method for crystallization of proteins. *J. Appl. Cryst.* **24,** 409–411 (1991).
34. Flot, D. *et al.* The ID23-2 structural biology microfocus beamline at the ESRF. *J. Synchrotron Radiat.* **17,** 107–118 (2010).
35. Kabsch, W. Xds. *Acta Crystallogr. D* **66,** 125–132 (2010).
36. Evans, P. Scaling and assessment of data quality. *Acta Crystallogr. D* **62,** 72–82 (2006).
37. Collaborative Computational Project, Number 4. The CCP4 suite: programs for protein crystallography. *Acta Crystallogr. D* **50,** 760–763 (1994).
38. McCoy, A. J. *et al.* Phaser crystallographic software. *J. Appl. Cryst.* **40,** 658–674 (2007).
39. Brünger, A. T. *et al.* Crystallography & NMR system: A new software suite for macromolecular structure determination. *Acta Crystallogr. D* **54,** 905–921 (1998).
40. Vagin, A. A. *et al.* REFMAC5 dictionary: organization of prior chemical knowledge and guidelines for its use. *Acta Crystallogr. D* **60,** 2184–2195 (2004).
41. Adams, P. D. *et al.* PHENIX: a comprehensive Python-based system for macromolecular structure solution. *Acta Crystallogr. D* **66,** 213–221 (2010).
42. Emsley, P. & Cowtan, K. Coot: model-building tools for molecular graphics. *Acta Crystallogr. D* **60,** 2126–2132 (2004).
43. Laskowski, R. A., MacArthur, M. W., Moss, D. S. & Thornton, J. M. PROCHECK: A program to check the stereochemical quality of protein structures. *Appl. Cryst.* **26,** 283–291 (1993).
44. Hooft, R. W., Vriend, G., Sander, C. & Abola, E. E. Errors in protein structures. *Nature* **381,** 272 (1996).
45. McDonald, I. K. & Thornton, J. M. Satisfying hydrogen bonding potential in proteins. *J. Mol. Biol.* **238,** 777–793 (1994).
46. Wallace, A. C., Laskowski, R. A. & Thornton, J. M. LIGPLOT: a program to generate schematic diagrams of protein-ligand interactions. *Protein Eng.* **8,** 127–134 (1995).
47. Krissinel, E. & Henrick, K. Inference of macromolecular assemblies from crystalline state. *J. Mol. Biol.* **372,** 774–797 (2007).
48. DeLano, W. L. The PyMOL Molecular Graphics System ⟨http://www.pymol.org⟩ (2002).